University of Arkansas, Fayetteville

ScholarWorks@UARK

5-2020

Peptoid and Antibody-based GFP Sensors

Solomon Isu
University of Arkansas, Fayetteville

Follow this and additional works at: https://scholarworks.uark.edu/etd

Part of the Amino Acids, Peptides, and Proteins Commons, Biochemical and Biomolecular Engineering Commons, Membrane Science Commons, and the Polymer and Organic Materials Commons

Peptoid and Antibody-based GFP Sensors

A thesis submitted in partial fulfillment
of the requirements for the degree of
Master of Science in Chemical Engineering

by

Solomon Isu
Federal University of Technology, Owerri
Bachelor of Engineering in Chemical Engineering, 2007
University of Salford
Master of Science in Petroleum/Gas Engineering, 2009

May 2020
University of Arkansas

This thesis is approved for recommendation to the Graduate Council

_____
Shannon Servoss, Ph.D.
Thesis Director

_____
Lauren Greenlee, Ph.D.
Committee member

_____
Ranil Wickramasinghe, Ph.D.
Committee member

_____
Julie Stenken, Ph.D.
Committee member

Abstract

In this work, we have made and characterized a pair of immunobiosensors for detecting the green fluorescent protein (GFP) in an aqueous matrix. An anti-GFP antibody-based biosensor was assembled to detect GFP, while a novel peptoid (N-substituted oligomers of glycine designated as IOS-1) biosensor was also assembled for GFP detection. A quartz crystal microbalance (QCM) gold sensor was used as the supporting substrate for self-assembly of the immunobiosensors. Gravimetric measurements of the QCM gold sensor during immunobiosensor construction and operation were available in real-time using a QCM instrument. X-ray photoelectron spectroscopy, Fourier transform infrared spectroscopy, and Fluorescence microscopy were used to characterize the immunobiosensors. Dose-dependent calibration curves were developed to contrast the performance of the peptoid immunobiosensor and the antibody-based immunobiosensor. The sensitivity of the biosensors shows that the peptoid could detect GFP at 8 nM, unlike the antibody immunobiosensor, which starts to measurably detect GFP at 40 nM. IOS-1 peptoid immunobiosensor had more adsorption capacity for GFP than the antibody-based immunobiosensor and could be reused through multiple adsorption/ desorption cycles. The peptoid immunobiosensor had a binding constant of 2.197×10^7 M^{-1} with GFP.

ACKNOWLEDGEMENTS

TABLE OF CONTENTS

LIST OF FIGURES

LIST OF TABLES

1. Introduction

Biosensors are becoming more significant at the nexus of medicine, nanotechnology, and engineering. More rapid diagnostic kits are getting pushed into the market yearly. These biosensor-based devices are competing on several fronts, including the cost of production, reusability, robustness, precision, and simplicity. The proximity of disease testing/diagnosis to the prospective patient accredits a point-of-care testing (POCT) system.[1] Portable, stand-alone biosensors have advanced the POCT industry. Antibody conjugated immunobiosensors are highly specific in antigen detection, but high production costs and non-robustness are significant drawbacks.[2-5] Also, current immunoassaying techniques require significant skilled human resource and introduce a lag time before confirmation of ailments at diagnostic facilities.[4] Techniques commonly used in precise detection and quantification of antigens include high-performance liquid chromatography (HPLC), liquid chromatography in tandem with electrospray ionization mass spectrometry (LC-ESI-MS), and enzyme-linked immunosorbent assay (ELISA). Biosensors incorporating proteins have also found applications as early warning systems for such health hazards as cyanide ingress.[6] Apart from antibodies, other popular bioreceptors employed in biosensing include aptamers, enzymes, deoxyribonucleic acids (DNA), ribonucleic acids (RNA), peptides, and peptoids. Transducing mechanisms for these biosensors include piezoelectric, optical, thermal and electrochemical means.[7]

The motivation for this work stems from the need to detect capsid proteins of viruses using non-immunoglobulin components and synthetic molecules. GFP and its cognate antibody are used as a ligand-receptor pair to compare the affinity of synthetic molecules (peptoid) to GFP. These peptoid molecules lack the batch-to-batch variations found in antibodies (due to post-translational modifications. Batch-to-batch homogeneity will ensure reproducible measurements and accuracy

of peptoid biosensors. Our hypothesis points towards hydrophobic interactions, hydrogen bonds and Van der Waal forces playing a role in peptoid-analyte complexes.

Peptoids are highly customizable oligomers of nitrogen substituted glycine which are functional replicas of peptides.[6, 8, 9] From a technical standpoint; peptoids are structural isomers of peptides.[10] Peptoid side chains are attached to the amide nitrogen(s) rather than the α-carbon(s), unlike peptide side chains which are attached to the α-carbons.[10-12] Peptoids possess the capacity to imitate the biochemical, mechanical, and morphological features of valuable biological materials.[11, 13, 14] Side-chain combinatorial libraries abound for selection in peptoid design leading to products with varied biomimetic functionalities in sensing, molecular scaffold-based, and drug delivery applications.[15] Peptoids are resistant to proteases/peptidases,[16] they cost less to synthesize than most proteins, and have a broader operational envelope due to the absence of quaternary structures as is seen in native proteins.[9, 10, 17, 18] The immunobiosensor of choice for this work is a peptoid which is designated as IOS-1 peptoid. (See Figure 1).

Quartz crystal microbalance (QCM) is a gravimetric measurement device that employs reverse piezoelectricity in measuring tiny changes in mass (nanograms) for a quartz crystal sensor placed in the device.[19] QCM is a non-invasive/non-destructive testing technique which reads out frequency changes in-lieu of mass loading for a piezoelectric quartz crystal in real-time.[20] The QCM has become a convenient device in biomolecular interaction analysis (BIA). With the versatility of QCM devices, nanoscale binding/unbinding events can be tracked more conveniently. The QCM has made it possible for bench-scale evaluation of bioanalytical performance of prospective biosensing materials. Disease-specific biomarkers in appropriate buffer solutions can be pumped across a microfluidic-sized QCM chamber containing a QCM sensor that has been surface modified with the antibody-surrogate of choice. Biorecognition and

specificity of bioanalytical interactions can be confirmed using characterization techniques. Ultra-sensitivity and low limits of detection characterize a perfect biosensor, and the QCM can provide the user with this information. Previous applications of the QCM in biosensing include protein and nucleic acid detection,[19, 21-24] bacteria detection,[25-27] cell surface interactions,[28, 29] and stem cell selection/extraction.[30]

There appears to be a knowledge gap in peptoid biosensing from a standalone perspective since most peptoid sensing work has explored conjugating peptoids to other organometallic agents as well as forming nanosheets and other tertiary structural forms. Antibody-surrogacy attributes of IOS-1 peptoid was illustrated through self-assembly of IOS-1 peptoid on the QCM gold sensor and subsequent capture of the analyte of choice. Previous work that points towards antibody surrogacy capabilities of peptoids include as a growth factor receptor (VEGFR2) antagonist,[16] amyloid-beta for Alzheimer's disease detection,[31] and lectin immobilization.[32]

This work demonstrates the immunobiosensing capability of IOS-1 peptoid in green fluorescent protein (GFP) detection and contrasted the performance of immunoglobulin (anti-GFP antibody) as a GFP biosensor. The presence of a lysine side chain in the peptoid structure in combination with other intermolecular forces are thought to play a role in GFP adsorption.[33-35] The peptoid immunobiosensor was shown to have the capacity to regenerate by using 0.1% sodium dodecyl sulfate (SDS) solution, rinsing with phosphate buffer (PBS) and adsorbing GFP.

Chapter 2

2.0 Materials and Methods

2.1 Materials and reagents

Tert-butyl N-(4-aminobutyl)carbamate was purchased from CNH technologies (Woburn, MA). Triisopropyl silane (TIS), (S)-(-)-α-methyl benzylamine and 2-aminoethanethiol hydrochloride were purchased from Acros Organics (Pittsburgh, PA). Piperidine and (S)-(+)-2-aminobutane were purchased from Alfa Aesar (Ward Hill, MA). Disuccinimidyl suberate and L-Cysteine were purchased from Thermo Fisher Scientific (Waltham, MA). MBHA rink amide resin and GFP were purchased from EMD Millipore (Burlington, MA). Anti-GFP (mouse) monoclonal antibody was purchased from Rockland antibodies and assays (Limerick, PA). Cr/Au coated QCM sensors were purchased from QuartzPro (Jarfalla, Sweden). All other reagents were purchased from VWR (Radnor, PA) and used without further modification. 18.2 MΩ ultrapure water was used in all instances.

2.2 Synthesis and purification of IOS-1 peptoid

Peptoids were synthesized via the sub-monomer solid-phase method on rink amide resin as earlier described.[14] In order to cause swelling of the resin beads, dimethylformamide (DMF) was used. A solution of 20% piperidine in DMF facilitated the removal of the protection group. Acylation of the secondary amine on the resin was carried out for one minute using a 5.3:1 volume ratio of 0.4 M bromoacetic acid (BAA) in DMF and N,N'-diisopropyl carbodiimide. An S_N2 nucleophilic substitution reaction was used to add amine sub-monomers with concentration ranging from 0.2 M to 1 M and a reaction time of one minute. Cyclic acylation and S_N2 reactions took place in order to attain the desired sequence of IOS-1 peptoid. The disconnection of IOS-1

peptoid from the solid resin beads was accomplished by suffusing in a solution of 95% trifluoroacetic acid (TFA), 2.5% water and 2.5% triisopropyl silane for five minutes. The TFA was removed using a Heidolph Laborota 4001 rotating evaporator (Elk Grove Village, IL), and the crude IOS-1 was weighed and stored at -20 °C.

Next, the IOS-1 peptoid was purified using a Waters preparative HPLC unit (Milford, MA) with a Duragel G C18 150 x 20 mm column (Peeke Scientific, Novato, CA). The preparative HPLC gradient started from 5% solvent B in A to 95% solvent B in A over 90 minutes (solvent A: water, 5% acetonitrile, and 0.1% TFA; solvent B: acetonitrile, 5% water, and 0.1% TFA). Crude IOS-1 peptoid was dissolved in a 50:50 solution of ultrapure water and acetonitrile to give a concentration value of 3 mg/ml. IOS-1 peptoid solution was fed into the preparative HPLC. Purified IOS-1 was confirmed to be higher than 98% pure via analytical HPLC (Waters Alliance) with a Duragel G C18 column (150 x 2.1 mm; Peeke Scientific). A linear gradient of 5% solvent D in C through 95% solvent D in C was run for 30 minutes (solvent C: water with 0.1% TFA; solvent D: acetonitrile with 0.1% TFA). A Matrix-Assisted Laser Desorption/Ionization Time-of-flight (MALDI-TOF) mass spectrometer (Bruker, Billerica, MA) was used to confirm the purified IOS-1 peptoid molecular weight matched the theoretical expected molecular weight (1364 g/mol). Purified IOS-1 was dried using a Labconco lyophilizer (Kansas City, MO) and stored at -20 °C.

2.3 QCM sensor modification

QCM gold (Au) sensors were prepared for modification by incubating in a UV/ozone chamber for 10 minutes. Subsequently, the Au sensor was cleaned with basic piranha solution (5 ml DI water; 1 ml of 30% H_2O_2 and 1 ml of 27% NH_4OH) at 73°C for 5 minutes. Ultrapure water was used to rinse the sensor before drying with nitrogen gas and incubating in a UV/ozone chamber for 10 minutes. QCM Au sensor was modified with IOS-1 peptoid via Au-thiol interaction; by

pipetting 100 µl of 25 µM IOS-1 peptoid solution in 50% water: 50% acetonitrile on the sensor surface and incubating for 90 minutes in the fume hood. Ultrapure water was used to rinse the sensor before drying with nitrogen. The cysteamine side chain of IOS-1 peptoid has a sulfhydryl group (-SH) that could become oxidized or deprotonated leading to covalent cross-linking with adjacent peptoids to form dimers through disulfide bonding. In order to mitigate dimerization, dilute solutions of IOS-1 peptoid (0.000025M) were used in a 50:50 solution of acetonitrile and water. The 50:50 solution, with a pH of 7, hinders deprotonation and dimerization.

A second Au sensor was cleaned as previously described for IOS-1 peptoid biosensors. Cysteamine was attached to the QCM Au sensor by pipetting 100 µl of 0.1 M cysteamine solution in DI water onto the sensor surface and setting the sensor in the fume hood for 4 hours before rinsing with DI water and drying with nitrogen. Au-thiol interaction was used to immobilize cysteamine on Au surface. Disuccinimidyl suberate (DSS) was used as a bifunctional linker to immobilize the antibody on the cysteamine-modified surface. A 0.5 mM solution of DSS in methanol was prepared immediately before use. The cysteamine-modified sensor was immersed in the DSS solution for 1 minute, rinsed with ethanol and dried with nitrogen gas. 170 µl of GFP antibody (0.3 µM) was pipetted on the sensor, incubated for 1 hour in the fume hood, rinsed with DI water and dried with nitrogen gas.

2.4 QCM measurement

Two gravimetric measurement modes were carried out using the QCM. Static measurements were for surface modification of the Au-plated quartz crystal. Dynamic, in-situ measurements were for the real-time detection of analyte capture and desorption from the immunobiosensor. Gravimetric analysis was carried out using a Biolin Scientific QSense analyzer (Gothenburg, Sweden). Cr/Au coated QCM 5 MHz sensors were surface modified and mounted

6

in a QSense flow cell. Flow cell tubing was connected to a QSense peristaltic pump and the analyte container. GFP (8 nM - 315 nM) in phosphate-buffered saline (PBS, pH 7.4) was used as the analyte fluid while PBS rinses were done before and after GFP flow to ensure consistent baselines for determination of the total adsorbed GFP. After the attachment of GFP, the fluid was switched to 0.1% sodium dodecyl sulfate (SDS) to desorb the adsorbed analyte. Flow rate, temperature, and flow cell volume were 100 µl/min, 23.3 °C and 40 µl, respectively. The frequency of a QCM sensor changes in response to mass transfer events on the sensor surface and viscosity variations between working fluids.[36] The frequency change applied for computing mass loadings was the third overtone. Flow duration of 20 minutes per solvent before taking endpoint measurements in PBS ensured frequency stabilization during flow. Sensor measurements were taken in the QCM cell to obtain the post-modification frequency before the flow of analyte solution across the sensor for real-time frequency measurement/monitoring of adsorptive and desorptive events.

Assessing the induced energy dissipation per unit mass attached helped determine if the adsorbed analyte tended towards a rigid film or a soft layer.[37] The absolute value of the slope for change in energy dissipation versus change in frequency during GFP capture was equal to 0.0297 ± 0.000224 (see Figure S11 in supplementary information). Energy dissipation versus frequency slope for a clean sensor was 0.0053 ± 0.00018 (see figure S9 in supplementary information). The value of these slopes are indicative of low dissipative effects (of soft and loosely attached molecules) on the biosensor and helped conclude whether the Sauerbrey model would suffice.[38-40] A covalently immobilized protein generally induces less dissipation than physically adsorbed proteins.[41, 42] Slope values when GFP is immobilized is of the same order of magnitude as a clean sensor (a gradient ratio of 6:1) and as such the Sauerbrey model was deemed to compute mass loading on the sensor accurately. A close approximation between the mass of adsorbed peptoid to

7

the mass for a rigidly assembled monolayer further validates the Sauerbrey assumption for IOS-1 peptoid biosensing. The Sauerbrey model relates the frequency change of a QCM sensor to the mass change based on the assumption of rigid attachment of the biorecognition element to the sensor surface and even distribution of mass on the surface.

2.5 Fourier Transform infrared spectroscopy (FT-IR)

FT-IR is mostly applied for detecting organic samples and to a lesser extent, inorganic samples. A Perkin Elmer frontier FT-IR (Wellesley, MA) was used for measurements of immunobiosensor transmittance. A background scan was carried out before sensor placement. FT-IR force gauge was monitored until a value of 80 was obtained before spectral scanning was carried out between 600 and 4000cm^{-1}. FT-IR transmittance mode was applied using these settings: 8 scan accumulations and 16cm^{-1} scan resolution.

2.6 X-ray photoelectron spectroscopy (XPS)

A PHI 5000 VersaProbe (ULVAC-PHI, Kanagawa, Japan) was used for measurements. In order to take sample measurements, an ultra-high vacuum of 10^{-8} mbar was established before a spectral survey scan was carried out between 0 and 1200 eV binding energy. Detailed scans for the following components were carried out within the range of their binding energy peak values: carbon, nitrogen, and oxygen. The PHI MultiPack software was used to calculate the elemental composition of the samples from the peak areas.

Chapter 3

3.0 Results and discussion

3.1 Immobilization of Peptoid on Au QCM Sensor

IOS-1 peptoid was selected for biosensing studies because it had previously been shown to interact with beta-sheet containing proteins.[43] The sequence of IOS-1 peptoid side chains is shown in Figure 1 below.
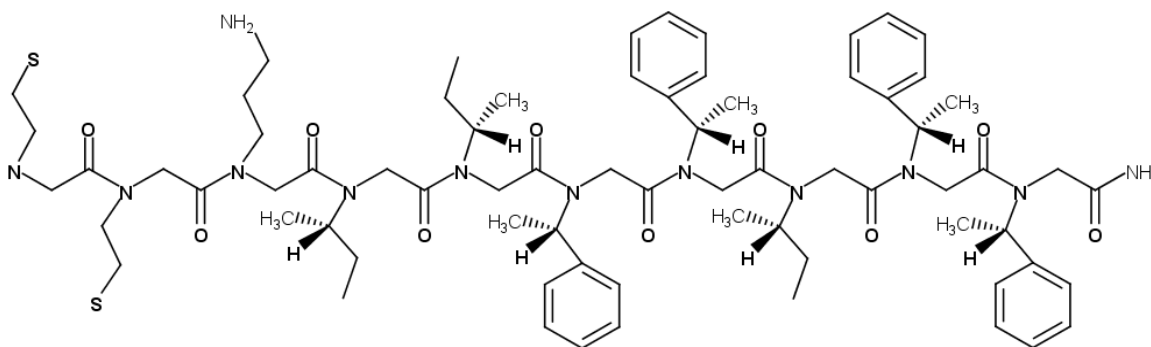
IOS-1 Peptoid
M.W. 1364 Da
Chemical formula: $C_{72}H_{106}N_{12}O_{10}S_2$

Figure 1. Chemical structure of IOS-1 peptoid

IOS-1 peptoid was attached to the Au sensor via thiol-Au interaction. Immobilization of IOS-1 peptoid on an Au sensor is shown in Figure 2A, with mass loading was 300.2 ng. Based on theoretical calculations for monolayer coverage of the QCM sensor with the peptoid, a theoretical mass loading of ~ 244 ng was anticipated (see Table S1, in supplementary information). The similarity between measured and theoretical values led to the assumption that IOS-1 peptoid was mainly a monolayer. The average amount of peptoid adsorbed on the sensor was 363.1 ng after ten repeats with a standard deviation of 98.5 ng. As can be seen in Figure 2B, the anti-GFP

antibody was immobilized on a QCM Au sensor. Adsorbed mass of cysteamine was 226.3 ng. The total mass loading of DSS and GFP antibody obtained was 682.7 ng.
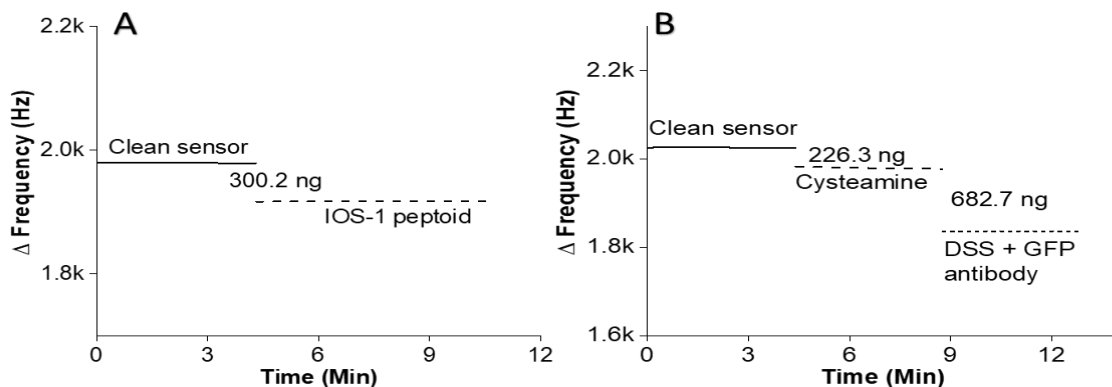
Figure 2. Representative surface modification experiments for self-assembled layers on Au sensor. using droplet incubation, rinsing, and N$_2$-drying. **(A)** IOS-1 peptoid **(B)** Cysteamine, DSS, and anti-GFP antibody. The experiments were repeated over ten times with a standard deviation of 60.

3.2 Surface characterization by XPS

XPS was used to characterize the immunobiosensor layers during fabrication and after GFP adsorption. Elemental compositions for peptoid and anti-GFP immunobiosensors are shown in Table 1 below. The elemental ratio of Au (Au4f) in the peptoid immunobiosensor decreased from 39.8% to 18.7% following GFP adsorption. Likewise, Au4f declined from 23.3% to 19.3% in the anti-GFP immunobiosensor following GFP adsorption. Au4f signal decline suggests that GFP adsorption on the immunobiosensors further blocks out the Au surface, thereby confirming the immobilization of GFP. A universal effect of adsorbed GFP on the immunobiosensor is the reduction of Au 4f photoelectron intensity. There was a significant decline in Au 4f signal in the peptoid immunobiosensor before and after GFP adsorption. GFP is bulkier than the peptoid and therefore, results in Au 4f signal decrease from 39.8% to 18.7% after adsorption on the peptoid.

On the antibody sensor, Au 4f declined by 3.7% after GFP adsorption because an anti-GFP antibody molecule weighs five times as much as a GFP molecule.

Table 1. A) Relative elemental composition of IOS-1 peptoid immunobiosensor and anti-GFP antibody immunobiosensor with and without attached GFP, as determined by XPS.
B) Relative elemental composition of IOS-1 peptoid immunobiosensor and anti-GFP antibody immunobiosensor with and without attached GFP neglecting Au 4f signal.

A	Elemental percentage (atom %)			
	O 1s	N 1s	C 1s	Au 4f
IOS-1 Peptoid	4.8	9.4	46.0	39.8
IOS-1 Peptoid + GFP	12.0	13.7	55.4	18.7
Antibody	15.0	11.6	50.4	23.0
Antibody + GFP	30.0	7.4	43.3	19.3

B	Elemental percentage (atom %)		
	O 1s	N 1s	C 1s
IOS-1 Peptoid	8.0	15.6	76.4
IOS-1 Peptoid + GFP	14.8	16.9	68.2
Antibody	19.5	15.1	65.5
Antibody + GFP	37.2	9.2	53.7

From Table 1A, the elemental percentage of O 1s on the peptoid surface increased from 4.8% to 12% after GFP attachment due to the carboxylic groups present in GFP but not present in the peptoid.[44] Likewise, GFP was diluted in PBS buffer, which contains phosphates and leads to an increase in O 1s ratio after GFP adsorption. The ratio of O 1s also increased from 15% to 30% on the anti-GFP surface following GFP adsorption. An increase occurred in the nitrogen (N 1s) ratio after GFP adsorption on the peptoid surface; however, a decrease occurred in the anti-GFP surface. These different trends in elemental ratios indicate changes in the surface chemistry of the samples.[45] A difference in the N 1s trend for the anti-GFP surface could be due to imprecise layer-by-layer surface modification of the anti-GFP immunobiosensor. Different sensors were used for

each measurement. Likewise, the percentage of C 1s increased from 46% to 55.4% on the peptoid surface while decreasing from 50.4% to 43.3% on the anti-GFP surface. XPS spectra suggest that the total organic content of the peptoid surface was 60.2% while total organic content of the anti-GFP surface was 77%.

Table 1B is necessitated by the fact that we have a layered structure on a gold surface. So, the differences in percentage Au 4f could be stemming from differences in thickness of the organic layer on top of the gold and hence the need to normalize the data. However, Table 1B shows similar trends to Table 1A with a few exceptions. The percentages change values after GFP adsorption were slightly different after normalizing the signals by excluding Au 4f though the trends stayed same. There is an 8.2% decrease in C 1s after GFP immobilization on the peptoid sensor when Au 4f is neglected unlike the 9.4% increase in C 1s when Au 4f is considered. The difference in C 1s trends for the peptoid sensor is due to the significant spectra of Au 4f in the peptoid-only sample.

Characterization experiments were focused on the peptoid sensor specifically, since the Au-alkane thiol-DSS approach for antibody immobilization is well-known and previously reported.[46-49] Detailed XPS spectra for the anti-GFP immunobiosensor is also shown in Figure S1, (supplementary information). The detailed XPS spectral scans for oxygen, nitrogen, and carbon before and after GFP attachment to the peptoid are shown in Figure 3A, 3B and 3D, respectively. Information in Figure 3C was extracted from the XPS survey scans (Figures S3 and S4, supplementary information) due to the significant intensity of the Au4f peak. As shown in Figure 3C, when GFP adsorbs to the peptoid immunobiosensor, Au4f intensity decreased from 120,000 counts per second to 70,000 counts per second. A decrease in Au 4f intensity suggests an increment in the mass of adsorbed material. The O 1s spectra for peptoid-only in Figure 3A has a single peak (centered at 531 eV) whose position fits oxygen present in amides.[50, 51] When GFP

adsorbed on the peptoid, a shoulder-peak occurred (centered at 535 eV) which represents oxygen present in hydroxide functional groups of carboxylic acids in amino acids.[51] IOS-1 peptoid does not possess carboxylic acids. The N 1s spectra in Figure 3B have just one peak centered at 400 eV and represent nitrogen that is present in amides and organic matrices.[50, 51] The C 1s spectra for peptoid-only and peptoid plus GFP in Figure 3D have shoulder peaks in addition to the central peaks. Central peaks for C 1s are centered at 285 eV and represent C-C bonds.[45, 52] The C 1s shoulder peaks in Figure 3D are centered at 288 eV and represent O-C=O and O=C-N present in GFP and IOS-1 peptoid, respectively.[51, 53]
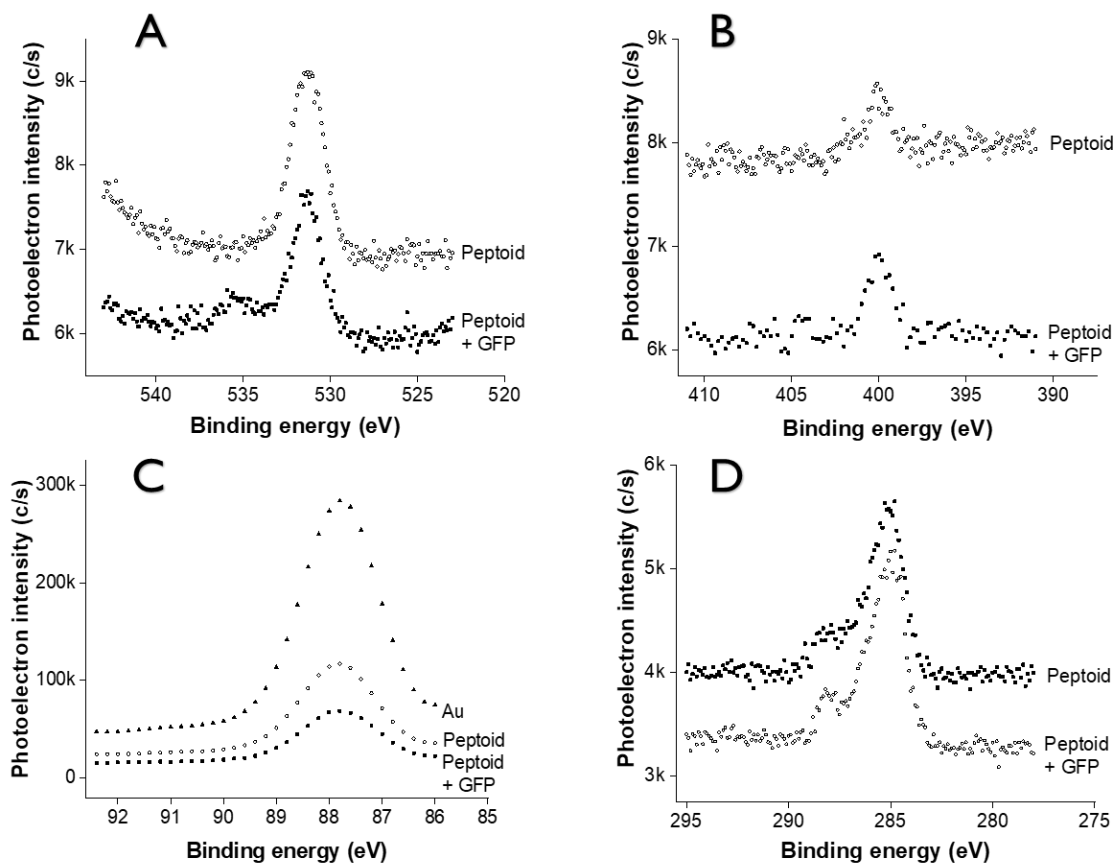

Figure 3. Detailed XPS spectra that compares surface chemistry for IOS-1 peptoid immunobiosensor before and after GFP immobilization. **(A)** oxygen (O1s), **(B)** nitrogen (N1s), **(C)** Au (Au4f), and **(D)** carbon (C1s).

3.3 Surface characterization by FT-IR

FT-IR spectral scans were carried out at the various stages of immunobiosensor fabrication and operation as illustrated by the composite spectra in Figure 4 below. Peak 1 represents O-H stretching vibrations[54] on the clean gold sensor either from silanol or ambient moisture, which is more likely. Peak 2 designates the C-H asymmetrical stretching found in alkanes[55] and is visible in all the observed spectra. Both the peptoid and GFP contain alkanes. The presence of alkanes on the gold sensor indicates some form of ambient contamination. Peak 3 signifies an S-H stretch with bonded thiols[56] and is unique to the immobilized peptoid via Au-S bonding. Peak 3 becomes attenuated when GFP adsorbs on the peptoid. Peak 4 represents the C=O stretching vibrations of the peptide bond and are characteristic of amide bonded solids.[55, 57] The FT-IR results suggest a higher percentage of C=O in the peptoid-only than when GFP adsorbs. The minor difference in C=O peak areas may also be due to the use of different sensors for the experiments. Peak 5 represents a primary N-H bending deformation[58] and is weakly shown on the peptoid surface as well as when GFP adsorbs on the peptoid. Peak 6 is indicative of CH_2 bending deformation[58] and is more pronounced on the peptoid surface than after GFP adsorption on the peptoid. Peak 7 represents C-O stretch in carboxylic acids[59] and is unique to GFP since IOS-1 peptoid does not contain carboxylic groups. Peak 8 represents alkyl C-N stretch.[55] Isobutylamine on the peptoid side chain makes C-N stretch significant for peptoid only.
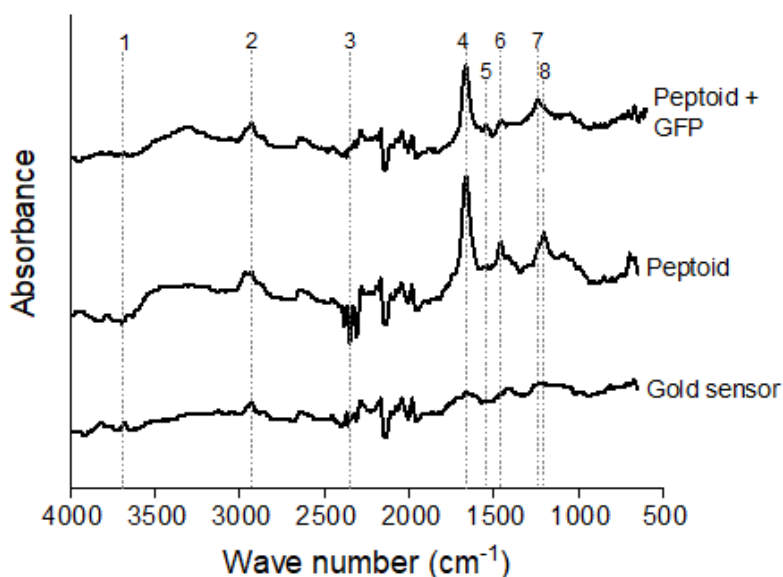
14

Figure 4. FTIR absorbance spectra for Au sensor, peptoid only and peptoid + GFP. Peak 1: 3667 cm⁻¹; Peak 2: 2929 cm⁻¹; Peak 3: 2348 cm⁻¹; Peak 4: 1664 cm⁻¹; Peak 5: 1549 cm⁻¹; Peak 6: 1461 cm⁻¹; Peak 7: 1241 cm⁻¹ and Peak 8: 1199 cm⁻¹.

3.4 Reversible GFP adsorption by immunobiosensor

The flow parameters used during analyte flow over the sensor resulted in Reynold's number of 3 within the QCM cell. A low Reynold's number mitigates mass transport disturbances and turbulence effects in the flow cell. The set flowrate enabled a turn-over time of 25 seconds through the flow cell, ensuring the quick introduction of new GFP solution. The mass loading of immobilized peptoid is directly proportional to the mass of analyte adsorbed, as shown in Figure S5 in the supplementary information. The Sauerbrey model was used for mass loading calculations because the rate of change in energy dissipation divided by the rate of change in sensor frequency was less than five percent. Figure 5A below illustrates the adsorption of GFP on the peptoid-modified Au sensor while Figure 5B shows a QCM Au sensor modified with a self-assembled monolayer of cysteamine, DSS and GFP antibody before the adsorption of GFP on the immunobiosensor.
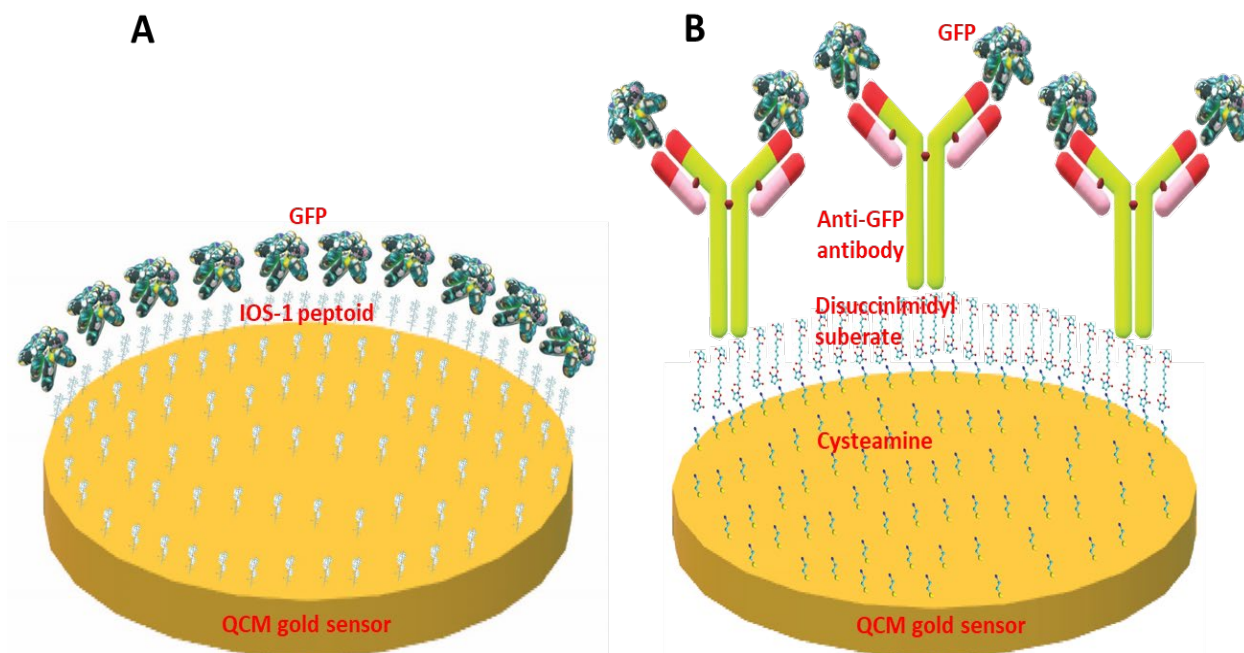
Figure 5. (A) Peptoid immunobiosensor. **(B)** Anti-GFP antibody immunobiosensor

The mass of GFP attached to IOS-1 peptoid immunobiosensor in Figure 6A below was found to be 166.3 ng. The amount of GFP that desorbed in Figure 6A, after the flow of 0.1% SDS/PBS solution, was also 166.3 ng. On the average, over 90% of adsorbed GFP was removed during SDS rinses. Complete desorption of GFP illustrated in Figure 6A indicates a peptoid biosensor that is reliable, and reproducible. The anti-GFP immunobiosensor in Figure 6B adsorbed 85 ng of GFP over 20 minutes. The antibody-based immunobiosensors adsorbed 65 ± 24 ng on average and about 80% was removed following the SDS wash. For the representative data shown in Figure 6B, 85 ng of GFP was adsorbed and 170% was removed due to the unfolding of antibody by SDS. Fluorescence microscopy images in Figure S8 (supplementary information) validate GFP capture on peptoid sensor. The functionality of IOS-1 peptoid immunobiosensor was retained after three SDS rinses, thereby making IOS-1 a viable candidate for immunobiosensing. Reusability data for IOS-1 peptoid is shown in Figure S6 (supplementary information). The reuse of anti-GFP

16

immunobiosensor was not achieved due to the functional degradation of anti-GFP antibody molecules by SDS rinses, as represented in Figure S7 (supplementary information).

The impact of electrostatic forces, as well as solvation and conformational entropy changes guiding protein adsorption onto sensor surfaces, imparts a degree of specificity to the peptoid-GFP interaction. Use of SDS rinses between measurements ensures reusability of peptoid immunobiosensor for multiple adsorption cycles.
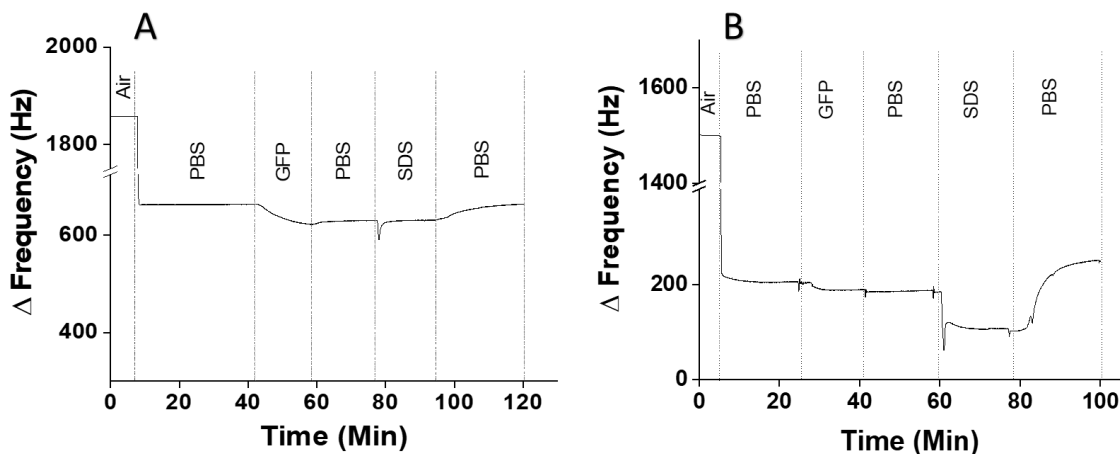
Figure 6. (A) Flow of PBS buffer, GFP, and SDS at 100 ul/min across IOS-1 peptoid immobilized on a QCM Au sensor. **(B)** Flow of PBS buffer, GFP and SDS at 100 ul/min across anti-GFP antibody immobilized on QCM Au sensor.

GFP adsorbed by the anti-GFP antibody, and peptoid immunobiosensors was observed to be directly related to initial GFP concentrations, as shown in Figure 7 below. Taking the superficial appearance of the GFP dose-response curves into consideration, the peptoid immunobiosensor demonstrates a negative exponential growth in GFP adsorbed as GFP concentration increases. Conversely, the anti-GFP immunobiosensor portrays a linear relationship between GFP adsorbed and initial GFP concentration.
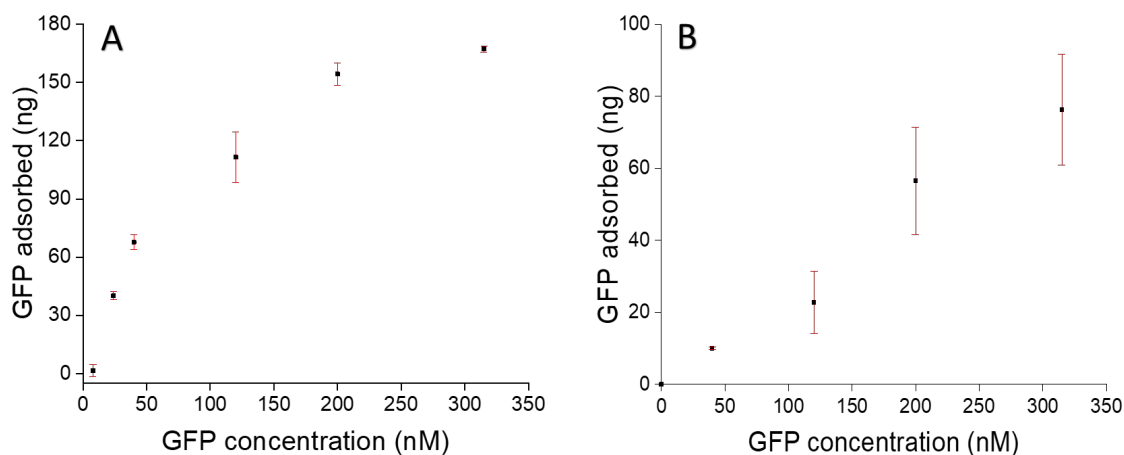
Figure 7. **(A)** GFP dose-dependency curve for peptoid immunobiosensor. **(B)** GFP dose-dependency curve for anti-GFP immunobiosensor.

At every GFP concentration in the calibration curves above, the peptoid adsorbed twice as much GFP as the anti-GFP antibody. The remarkable performance of the peptoid immunobiosensor can be attributed to the presence of more binding sites per unit area. The availability of binding sites per unit area is illustrated in Figures S12 and S13, supplementary information. Despite the advantage of IOS-1 peptoid over anti-GFP antibody, all the binding sites on the peptoid immunobiosensor cannot bind GFP on a 1:1 ratio because GFP is larger than the peptoid albeit smaller than the anti-GFP antibody.

Chapter 4

4.0 Electrochemistry of thiol and gold interactions

4.1 Background of electrochemical sensing

In order to complement the gravimetric detection of an analyte by the peptoid sensor, experiments were performed to evaluate the feasibility of performing electrochemical detection of thiol-gold binding interactions. IOS-1 peptoid self-assembles on the gold QCM sensor via the thiol side chains on the peptoid base. However, for proof-of-concept purposes, cysteine was used as a model molecule to study the thiol-gold electrochemical conjugation process. Cysteine is an essential amino acid in proteins and enzymes.[60] Gold-thiol nanoscale chemistry has been extensively studied in the past two decades,[60-63] and the unique bond strength has provided a template for many organometallic applications. Previous studies show that oxidizing the gold surface prior to thiol introduction enhances the self-assembly of thiols.[63]

Electrochemistry characterizes chemical processes by their electrical effects,[64] and is a useful tool in the study of nanoscale organometallic interactions between the working electrode and the analyte of interest in the electrolyte. Electrodes can be understood simply as an electrical conductor immersed in a conductive liquid solution (electrolyte). The combination is referred to as an electrochemical cell. A potentiostat and software analysis tools are used together to induce and detect electrical charges emanating from the electrochemical cell. The versatility of electrochemical techniques enables monitoring of oxidation and reduction processes, mass transport and diffusivity parameters, as well as adsorption and desorption phenomena.[65] Electrochemical techniques can yield very specific information and the electroanalytical methods we used were cyclic voltammetry (CV) and differential pulse voltammetry (DPV).

4.2 Cyclic Voltammetry Data

In cyclic voltammetry, the direction of the potential scan is inverted at the end of the forward sweep as well as at the end of the backward sweep to elucidate the chemical reaction cyclically. To perform cyclic voltammetry, the QCM electrochemical cell was mounted with clean gold sensors within. The process of UV/ozone cleaning oxidized the gold surface. The working electrode was the QCM gold sensor, the counter electrode was an in-built platinum electrode within the QCM cell, and the reference electrode was a world precision dri-ref electrode (3M KCl) equivalent to the silver-silver chloride reference electrode. The electrolyte used was phosphate-buffered saline (PBS, pH 7.4). Cysteine solutions of 1 µM, 5 µM, 10 µM, and 50 µM in PBS were used to obtain the binding curve. The scan rate was 50mV/s. Figure 8A below shows the cyclic voltammograms for 1 µM, 5 µM, 10 µM and 50 µM cysteine in PBS and there is a positive correlation between oxidative peak current height and cysteine concentration. The heights of the peak currents from the voltammograms were used to construct the calibration curves in Figure 8B below.
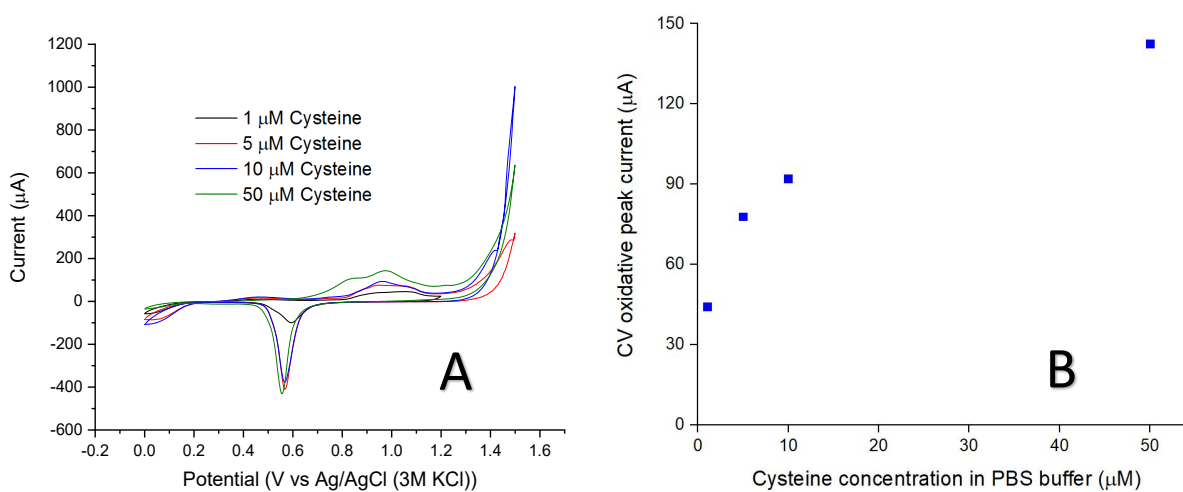

Figure 8. (A) Cyclic voltammograms for cysteine in 0.1 M PBS at varying concentrations. **(B)** Calibration curve of cyclic voltammogram peak currents versus cysteine concentration.

Cysteine adsorption to gold is postulated as a one-step oxidative process.[66] Proton coupled electron transfer is reported during electrochemical oxidation of cysteine.[60] Reversibility of the cysteine-gold reaction is demonstrated by the presence of forward and reverse peaks. Another fact that stands out in the CVs is that the forward sweep has two peaks (central peak at 1V and a shoulder peak at 0.85V) while the return sweep has only one peak at 0.55V. Applied voltage in the forward sweep appears to first cleave cysteine dimers (cystine) before adsorption of free sulfhydryl groups on gold (main peak). In the reverse step, there is only reduction and consequent desorption of monomeric cysteine species leading to just one peak.

4.3 Differential Pulse Voltammetry Data

As the title implies, differential pulse voltammetry uses the differential value of the current in order to increase the sensitivity of the technique in comparison to cyclic voltammetry and normal pulse voltammetry.[64] DPVs have a limit of detection up to 10^{-8} M unlike CVs. The voltammograms of cysteine using DPV at pH 7.4 and pH 8.2 are shown in Figures 9A and 9B respectively. The data in Figure 9A suggest the presence of buffer redox species having a significant oxidation peak at 0.4V at pH 7.4. The peak from the redox species in the buffer becomes muted at pH 8.2 in Figure 9B. The central peak in Figure 9A at 0.95V shows increasing peak heights for increasing cysteine concentrations and the shoulder peaks suggest cleavage of the disulfide bonds in cystine. As seen in Figure 9B, peak onset potential reduces as pH goes up. The main peaks in Figure 9B are centered at 0.85V (pH 8.2) in contrast with 0.95V (pH 7.4, Figure 9A) for the redox species. Onset potential shift with pH is a trend which has been previously reported.[60]
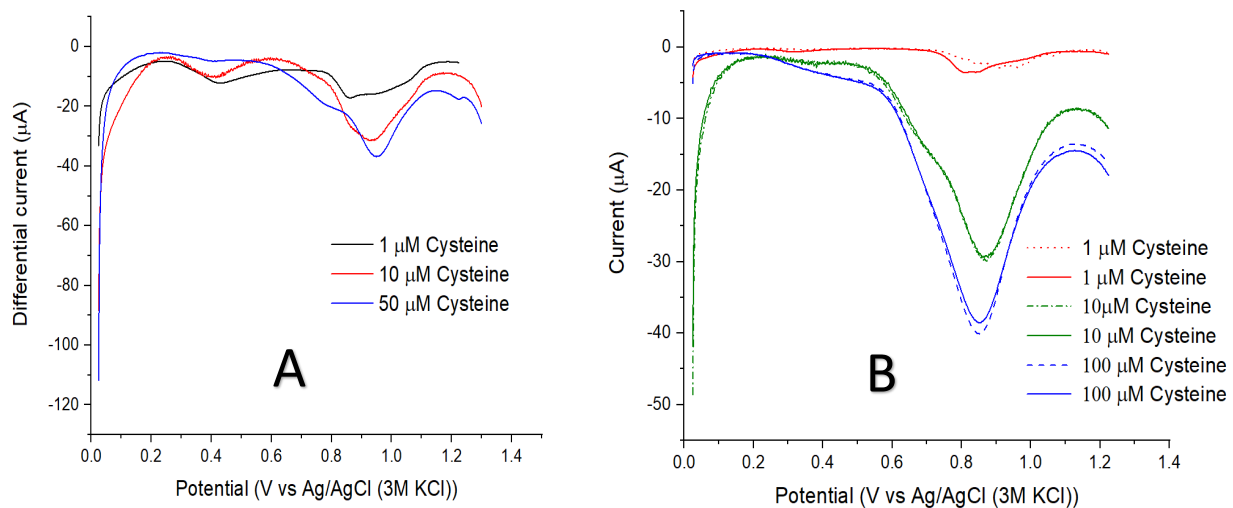
Figure 9. (A) Differential pulse voltammogram of varying cysteine concentrations in 0.1 M PBS at pH 7.4. **(B)** Differential pulse voltammogram of varying cysteine concentrations in 0.1 M PBS at pH 8.2.

Having demonstrated the concept of cysteine adsorption to gold by electrochemical means, the next step would be to design a template for electrochemical detection of peptoid self-assembly on gold and GFP capture on the peptoid-modified gold surface.

Conclusion

In this work, IOS-1 peptoid is shown to be a credible biomimetic agent for the detection of GFP. Previous efforts have explored 3D nanostructures of peptoids acting as a co-catalyst in biosensors as well as peptoid nanosheets as antibody surrogates.[15, 31, 67] Conversely, IOS-1 peptoid was not incorporated into a multi-component metalloorganic matrix. These results show that GFP mass loading is directly proportional to the GFP concentration in the sample solution. IOS-1 peptoid immunobiosensor was shown to possess over thrice as many GFP binding sites per unit area than anti-GFP immunoglobulin biosensors. (See Figures 15 and 16 in the supplementary information). The ability of the IOS-1 peptoid immunobiosensor to functionally regenerate was demonstrated by exposure to a solution of 0.1% SDS for 20 minutes during which time the adsorbed GFP desorbs. Subsequently, the peptoid immunobiosensor was used for GFP adsorption after rinsing with PBS buffer and without removal from the QCM device. Future work can focus on the design and synthesis of a suite of functionally significant peptoids for unique fingerprinting of biological analytes and subsequent analysis using energy dissipation and viscoelastic modeling in addition to pattern recognition software.

References

1.   Vashist, S. K., Point-of-Care Diagnostics: Recent Advances and Trends. *Biosensors (Basel)* **2017,** *7* (4).

2.   Olivier, G. K.; Cho, A.; Sanii, B.; Connolly, M. D.; Tran, H.; Zuckermann, R. N., Antibody-mimetic peptoid nanosheets for molecular recognition. *ACS Nano* **2013,** *7* (10), 9276-86.

3.   Weckman, N. E.; McRae, C.; Ko Ferrigno, P.; Seshia, A. A., Comparison of the specificity and affinity of surface immobilised Affimer binders using the quartz crystal microbalance. *Analyst* **2016,** *141* (22), 6278-6286.

4.   Ertekin, Ö.; Öztürk, S.; Öztürk, Z. Z., Label Free QCM Immunobiosensor for AFB1 Detection Using Monoclonal IgA Antibody as Recognition Element. *Sensors (Basel)* **2016,** *16* (8).

5.   Pirinçci, Ş.; Ertekin, Ö.; Laguna, D. E.; Özen, F.; Öztürk, Z. Z.; Öztürk, S., Label-Free QCM Immunosensor for the Detection of Ochratoxin A. *Sensors (Basel)* **2018,** *18* (4).

6.   Lim, B.; Lee, J., A Peptoid-Based Fluorescent Sensor for Cyanide Detection. *Molecules* **2016,** *21* (3), 339.

7.   Yoon, J. Y., *Introduction to biosensors: From electric circuits to immunosensors*. 2013; p 1-262.

8.   Zuckermann, R. N., Peptoid origins. *Biopolymers* **2011,** *96* (5), 545-55.

9.   Sun, J.; Zuckermann, R. N., Peptoid Polymers: A Highly Designable Bioinspired Material. *ACS Nano* **2013,** *7* (6), 4715-4732.

10.   Perez Bakovic, G. R.; Roberts, J. L.; Colford, B.; Joyce, M.; Servoss, S. L., Peptoid microsphere coatings: The effects of helicity, temperature, pH, and ionic strength. *Biopolymers* **2019,** *110* (6), e23283.

11.   Lau, K. H. A., Peptoids for biomaterials science. *Biomaterials Science* **2014,** *2* (5), 627-633.

12.   Rotem, S.; Mor, A., Antimicrobial peptide mimics for improved therapeutic properties. *Biochimica et Biophysica Acta (BBA) - Biomembranes* **2009,** *1788* (8), 1582-1592.

13.   Ganesh, S. D.; Saha, N.; Zandraa, O.; Zuckermann, R. N.; Saha, P., Peptoids and polypeptoids: biomimetic and bioinspired materials for biomedical applications. *Polymer Bulletin* **2017,** *74* (8), 3455-3466.

14.   Zuckermann, R. N.; Kerr, J. M.; Kent, S. B. H.; Moos, W. H., Efficient method for the preparation of peptoids [oligo(N-substituted glycines)] by submonomer solid-phase synthesis. *Journal of the American Chemical Society* **1992,** *114* (26), 10646-10647.

15.   Culf, A. S., Peptoids as tools and sensors. *Biopolymers* **2019**, e23285.

16.   Udugamasooriya, D. G.; Dineen, S. P.; Brekken, R. A.; Kodadek, T., A Peptoid "Antibody Surrogate" That Antagonizes VEGF Receptor 2 Activity. *Journal of the American Chemical Society* **2008,** *130* (17), 5744-5752.

17.   Della Ventura, B.; Iannaccone, M.; Funari, R.; Pica Ciamarra, M.; Altucci, C.; Capparelli, R.; Roperto, S.; Velotta, R., Effective antibodies immobilization and functionalized nanoparticles in a quartz-crystal microbalance-based immunosensor for the detection of parathion. *PLoS One* **2017,** *12* (2), e0171754.

18.   Lin, P. H.; Huang, S. C.; Chen, K. P.; Li, B. R.; Li, Y. K., Effective Construction of a High-Capacity Boronic Acid Layer on a Quartz Crystal Microbalance Chip for High-Density Antibody Immobilization. *Sensors (Basel)* **2018,** *19* (1).

19.   Sun, W.; Song, W.; Guo, X.; Wang, Z., Ultrasensitive detection of nucleic acids and proteins using quartz crystal microbalance and surface plasmon resonance sensors based on target-triggering multiple signal amplification strategy. *Anal Chim Acta* **2017,** *978*, 42-47.

20.   Rehman, A.; Zeng, X., Monitoring the Cellular Binding Events with Quartz Crystal Microbalance (QCM) Biosensors. *Methods Mol Biol* **2017,** *1572*, 313-326.

21.   Pohanka, M., Piezoelectric biosensor for the determination of Tumor Necrosis Factor Alpha. *Talanta* **2018,** *178*, 970-973.

22.   Sönmezler, M.; Özgür, E.; Yavuz, H.; Denizli, A., Quartz crystal microbalance based histidine sensor. *Artif Cells Nanomed Biotechnol* **2019,** *47* (1), 221-227.

23.   Mujahid, A.; Mustafa, G.; Dickert, F. L., Label-Free Bioanalyte Detection from Nanometer to Micrometer Dimensions-Molecular Imprinting and QCMs. *Biosensors (Basel)* **2018,** *8* (2).

24.   Han, Z.; Wang, Y.; Duan, X., Biofunctional polyelectrolytes assembling on biosensors - A versatile surface coating method for protein detections. *Anal Chim Acta* **2017,** *964*, 170-177.

25.   Farka, Z.; Kovář, D.; Skládal, P., Rapid detection of microorganisms based on active and passive modes of QCM. *Sensors (Basel)* **2014,** *15* (1), 79-92.

26.   Farooq, U.; Yang, Q.; Ullah, M. W.; Wang, S., Bacterial biosensing: Recent advances in phage-based bioassays and biosensors. *Biosens Bioelectron* **2018,** *118*, 204-216.

27.   Olsson, A. L.; Wargenau, A.; Tufenkji, N., Optimizing Bacteriophage Surface Densities for Bacterial Capture and Sensing in Quartz Crystal Microbalance with Dissipation Monitoring. *ACS Appl Mater Interfaces* **2016,** *8* (22), 13698-706.

28.   Pirich, C. L.; de Freitas, R. A.; Torresi, R. M.; Picheth, G. F.; Sierakowski, M. R., Piezoelectric immunochip coated with thin films of bacterial cellulose nanocrystals for dengue detection. *Biosens Bioelectron* **2017,** *92*, 47-53.

29.   Kilic, A.; Kok, F. N., Quartz crystal microbalance with dissipation as a biosensing platform to evaluate cell-surface interactions of osteoblast cells. *Biointerphases* **2017,** *13* (1), 011001.

30.   Maglio, O.; Costanzo, S.; Cercola, R.; Zambrano, G.; Mauro, M.; Battaglia, R.; Ferrini, G.; Nastri, F.; Pavone, V.; Lombardi, A., A Quartz Crystal Microbalance Immunosensor for Stem Cell Selection and Extraction. *Sensors (Basel)* **2017,** *17* (12).

31.   Zhu, L.; Zhao, Z.; Cheng, P.; He, Z.; Cheng, Z.; Peng, J.; Wang, H.; Wang, C.; Yang, Y.; Hu, Z., Antibody-Mimetic Peptoid Nanosheet for Label-Free Serum-Based Diagnosis of Alzheimer's Disease. *Adv Mater* **2017,** *29* (30).

32.   Battigelli, A.; Kim, J. H.; Dehigaspitiya, D. C.; Proulx, C.; Robertson, E. J.; Murray, D. J.; Rad, B.; Kirshenbaum, K.; Zuckermann, R. N., Glycosylated Peptoid Nanosheets as a Multivalent Scaffold for Protein Recognition. *ACS Nano* **2018,** *12* (3), 2455-2465.

33.   Bratek-Skicki, A.; Cristaudo, V.; Savocco, J.; Nootens, S.; Morsomme, P.; Delcorte, A.; Dupont-Gillain, C., Mixed Polymer Brushes for the Selective Capture and Release of Proteins. *Biomacromolecules* **2019,** *20* (2), 778-789.

34.   Rabe, M.; Verdes, D.; Seeger, S., Understanding protein adsorption phenomena at solid surfaces. *Advances in colloid and interface science 162* (1-2), 87-106.

35.   Somasundaran, P.; Huang, L., Adsorption/aggregation of surfactants and their mixtures at solid-liquid interfaces. *Advances in colloid and interface science 88* (1-2), 179-208.

36.   Dixon, M. C., Quartz crystal microbalance with dissipation monitoring: enabling real-time characterization of biological materials and their interactions. *J Biomol Tech* **2008,** *19* (3), 151-8.

37.   Gutman, J.; Walker, S. L.; Freger, V.; Herzberg, M., Bacterial attachment and viscoelasticity: physicochemical and motility effects analyzed using quartz crystal microbalance with dissipation (QCM-D). *Environ Sci Technol* **2013,** *47* (1), 398-404.

38.   Feiler, A. A.; Sahlholm, A.; Sandberg, T.; Caldwell, K. D., Adsorption and viscoelastic properties of fractionated mucin (BSM) and bovine serum albumin (BSA) studied with quartz crystal microbalance (QCM-D). *J Colloid Interface Sci* **2007,** *315* (2), 475-81.

39.   Olsson, A. L. J.; van der Mei, H. C.; Busscher, H. J.; Sharma, P. K., Novel Analysis of Bacterium−Substratum Bond Maturation Measured Using a Quartz Crystal Microbalance. *Langmuir* **2010,** *26* (13), 11113-11117.

40.   Schofield, A. L.; Rudd, T. R.; Martin, D. S.; Fernig, D. G.; Edwards, C., Real-time monitoring of the development and stability of biofilms of Streptococcus mutans using the quartz crystal microbalance with dissipation monitoring. *Biosens Bioelectron* **2007,** *23* (3), 407-13.

41.   Cooper, M. A.; Singleton, V. T., A survey of the 2001 to 2005 quartz crystal microbalance biosensor literature: applications of acoustic physics to the analysis of biomolecular interactions. *J Mol Recognit* **2007,** *20* (3), 154-84.

42.   Su, X.; Zong, Y.; Richter, R.; Knoll, W., Enzyme immobilization on poly(ethylene-co-acrylic acid) films studied by quartz crystal microbalance with dissipation monitoring. *J Colloid Interface Sci* **2005,** *287* (1), 35-42.

43.   Turner, J. P.; Lutz-Rechtin, T.; Moore, K. A.; Rogers, L.; Bhave, O.; Moss, M. A.; Servoss, S. L., Rationally designed peptoids modulate aggregation of amyloid-beta 40. *ACS Chem Neurosci* **2014,** *5* (7), 552-8.

44.   Takei, K.-i.; Takahashi, R.; Noguchi, T., Correlation between the Hydrogen-Bond Structures and the C═O Stretching Frequencies of Carboxylic Acids as Studied by Density Functional Theory Calculations: Theoretical Basis for Interpretation of Infrared Bands of Carboxylic Groups in Proteins. *The Journal of Physical Chemistry B* **2008,** *112* (21), 6725-6731.

45.   McArthur, S. L.; Mishra, G.; Easton, C. D., Applications of XPS in Biology and Biointerface Analysis. In *Surface Analysis and Techniques in Biology*, Smentkowski, V. S., Ed. Springer International Publishing: Cham, 2014; pp 9-36.

46.   Le Brun, A. P.; Soliakov, A.; Shah, D. S.; Holt, S. A.; McGill, A.; Lakey, J. H., Engineered self-assembling monolayers for label free detection of influenza nucleoprotein. *Biomed Microdevices* **2015,** *17* (3), 9951.

47.   Pham, V. B.; Phan, T. N. K.; Nguyen, T. T.; Pham, X. T. T.; Le, T. T. T.; Dang, M. C., Surface modification of a gold-coated microcantilever and application in biomarker detection. *Advances in Natural Sciences: Nanoscience and Nanotechnology* **2015,** *6* (4), 045018.

48.   Vashist, S. K.; Dixit, C. K.; MacCraith, B. D.; O'Kennedy, R., Effect of antibody immobilization strategies on the analytical performance of a surface plasmon resonance-based immunoassay. *Analyst* **2011,** *136* (21), 4431-6.

49.   Wiseman, M. E.; Frank, C. W., Antibody adsorption and orientation on hydrophobic surfaces. *Langmuir* **2012,** *28* (3), 1765-74.

50.   Hurisso, B. B.; Lovelock, K. R.; Licence, P., Amino acid-based ionic liquids: using XPS to probe the electronic environment via binding energies. *Phys Chem Chem Phys* **2011,** *13* (39), 17737-48.

51.   Stevens, J. S.; de Luca, A. C.; Pelendritis, M.; Terenghi, G.; Downes, S.; Schroeder, S. L. M., Quantitative analysis of complex amino acids and RGD peptides by X-ray photoelectron spectroscopy (XPS). *Surface and Interface Analysis* **2013,** *45* (8), 1238-1246.

52.   Iucci, G.; Battocchio, C.; Dettin, M.; Ghezzo, F.; Polzonetti, G., An XPS study on the covalent immobilization of adhesion peptides on a glass surface. *Solid State Sciences* **2010,** *12* (11), 1861-1865.

53.   Wallart, X.; Henry de Villeneuve, C.; Allongue, P., Truly quantitative XPS characterization of organic monolayers on silicon: study of alkyl and alkoxy monolayers on H-Si(111). *J Am Chem Soc* **2005,** *127* (21), 7871-8.

54.   Isernia, L., FTIR Study of the Relation, between Extra-framework Aluminum Species and the Adsorbed Molecular Water, and its Effect on the Acidity in ZSM-5 Steamed Zeolite. *Materials Research* **2013,** *16*, 792.

55.   Sandoval, S.; Kumar, N.; Oro-Solé, J.; Sundaresan, A.; Rao, C. N. R.; Fuertes, A.; Tobias, G., Tuning the nature of nitrogen atoms in N-containing reduced graphene oxide. *Carbon* **2016,** *96*, 594-602.

56.   Ko, D.; Lee, J. S.; Patel, H.; Jakobsen, M.; Hwang, Y.; Yavuz, C.; Hansen, H.; Andersen, H., Selective removal of heavy metal ions by disulfide linked polymer networks. *Journal of Hazardous Materials* **2017,** *332*.

57.   Steiner, G.; Tunc, S.; Maitz, M.; Salzer, R., Conformational Changes during Protein Adsorption. FT-IR Spectroscopic Imaging of Adsorbed Fibrinogen Layers. *Analytical Chemistry* **2007,** *79* (4), 1311-1316.

58.   Pu, Q.; Han, L.; Liu, X., Discrimination of different processed animal proteins (PAPs) by FT-IR spectroscopy based on their fat characteristics. *Biotechnology, Agronomy and Society and Environment* **2014,** *18*, 321-328.

59.   Arjunan, V.; Raj, A.; Mythili, C. V.; Mohan, S., Vibrational, electronic and quantum chemical studies of 5-benzimidazole carboxylic acid. *Journal of Molecular Structure* **2013,** *1036*, 326-340.

60.   Dey, M. K.; Kumar, S.; Satpati, A. K., Probing adsorptive/desorptive redox processes and detection of cysteine: A voltammetric and scanning electrochemical microscopy study. *Journal of Electroanalytical Chemistry* **2017,** *807*, 119-127.

61.   Hakkinen, H., The gold-sulfur interface at the nanoscale. *Nat Chem* **2012,** *4* (6), 443-55.

62.   Love, J. C.; Estroff, L. A.; Kriebel, J. K.; Nuzzo, R. G.; Whitesides, G. M., Self-Assembled Monolayers of Thiolates on Metals as a Form of Nanotechnology. *Chemical Reviews* **2005,** *105* (4), 1103-1170.

63.   Xue, Y.; Li, X.; Li, H.; Zhang, W., Quantifying thiol-gold interactions towards the efficient strength control. *Nat Commun* **2014,** *5*, 4348.

64.   Bard, A.; Faulkner, L., *Electrochemical Methods: Fundamentals and Applications, New York: Wiley, 2001, 2nd ed*. 2002; Vol. 38, p 1364-1365.

65.   Rajeshwar, K.; Ibanez, J. G.; Swain, G. M., Electrochemistry and the environment. *Journal of Applied Electrochemistry* **1994,** *24* (11), 1077-1091.

66.   Wang, L. H.; Huang, W. S., Electrochemical oxidation of cysteine at a film gold modified carbon fiber microelectrode its application in a flow-through voltammetric sensor. *Sensors (Basel)* **2012,** *12* (3), 3562-77.

67.   Ford, B. K.; Hamza, M.; Rabenstein, D. L., Design, synthesis, and characterization of heparin-binding peptoids. *Biochemistry* **2013,** *52* (21), 3773-80.

Appendices

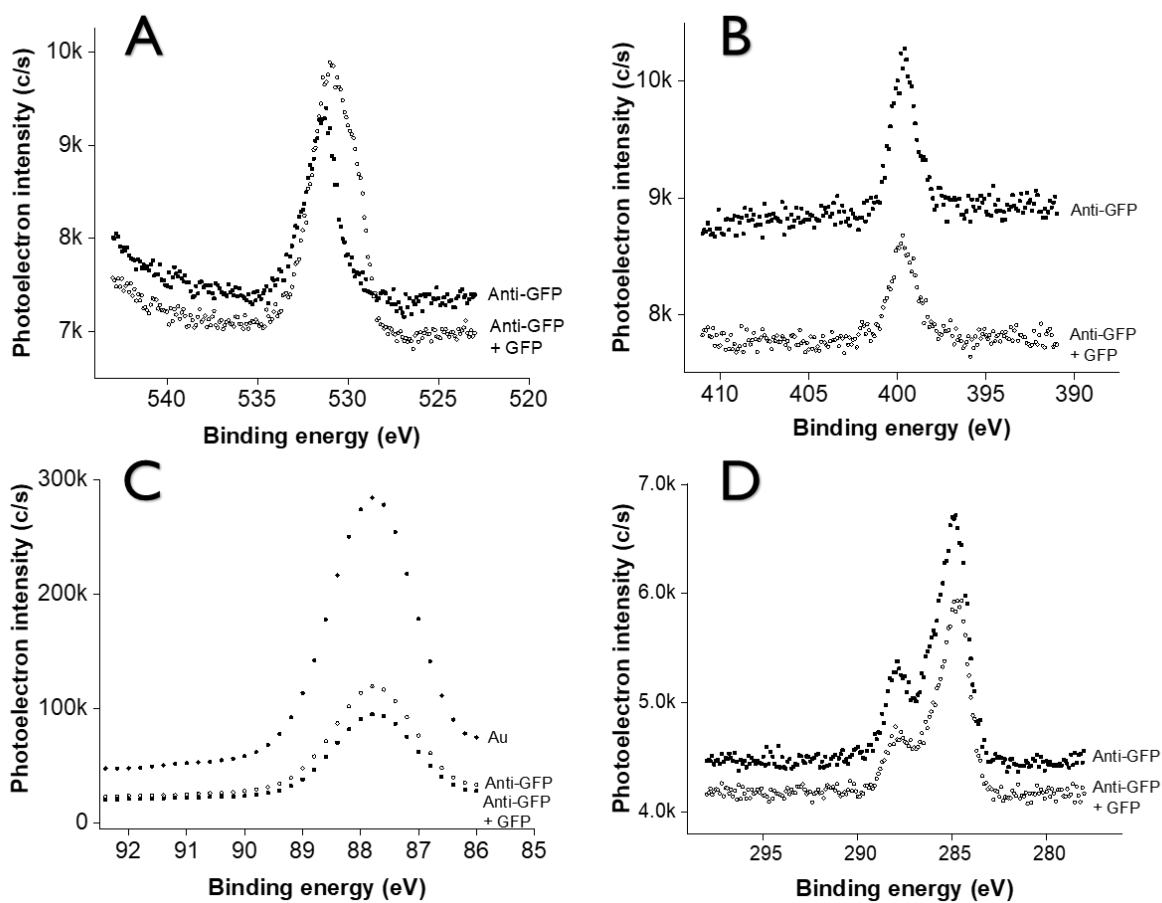## Supplementary Information

Figure S1. Detailed XPS spectra that compares surface chemistry for the anti-GFP immunobiosensor before and after GFP immobilization. **(A)** oxygen (O1s), **(B)** nitrogen (N1s), **(C)** Au (Au4f), and **(D)** carbon (C1s).
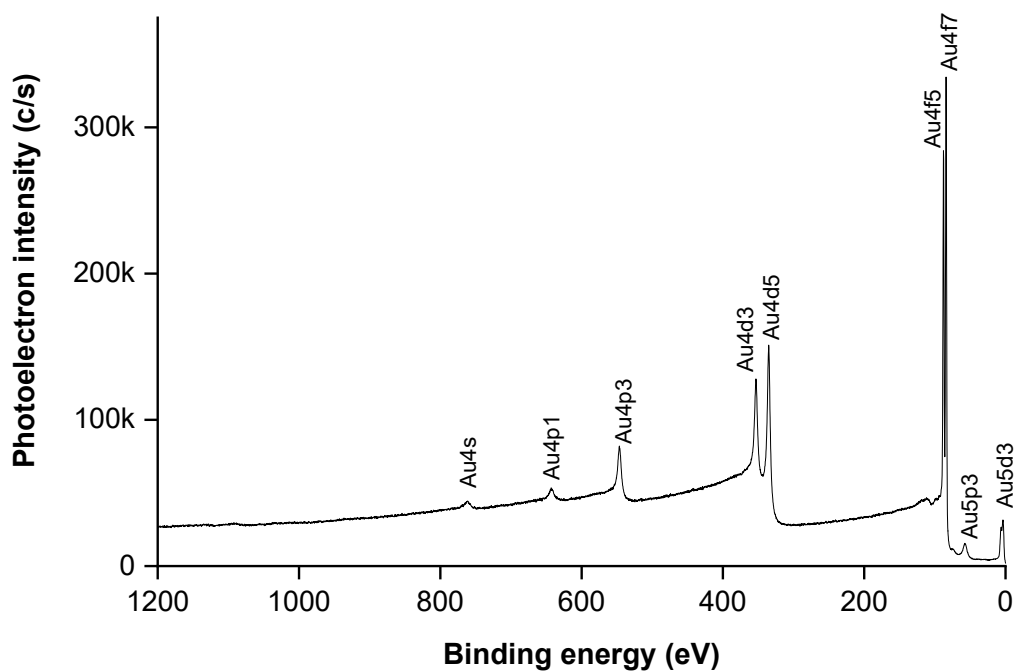
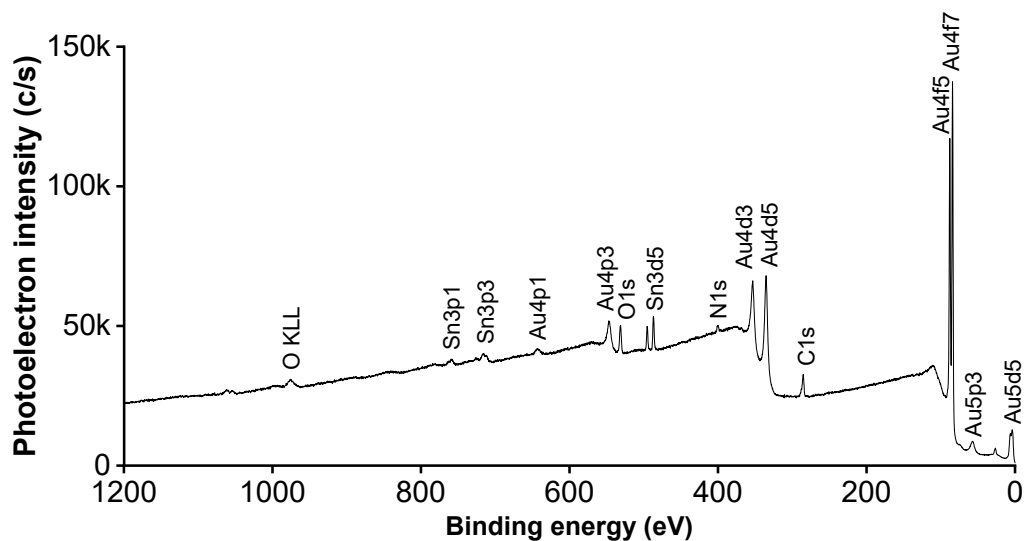**Figure S2**. XPS survey spectra of clean Au sensor following sputtering for 1 minute

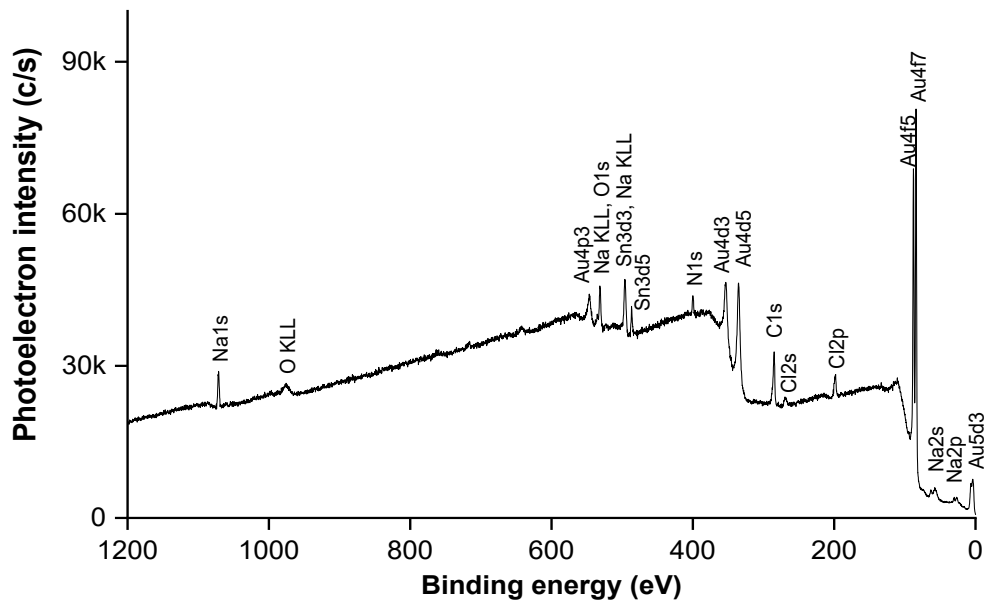**Figure S3**. XPS survey spectra of IOS-1 peptoid immobilized on QCM Au sensor

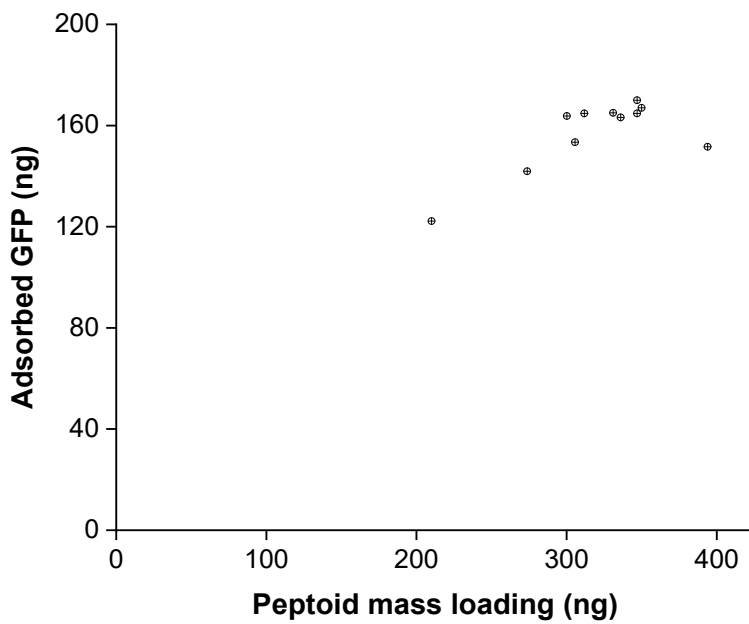**Figure S4**. XPS survey spectra of IOS-1 peptoid and GFP on QCM Au sensor

Figure S5. Relationship between mass loading of peptoid and GFP adsorbed.
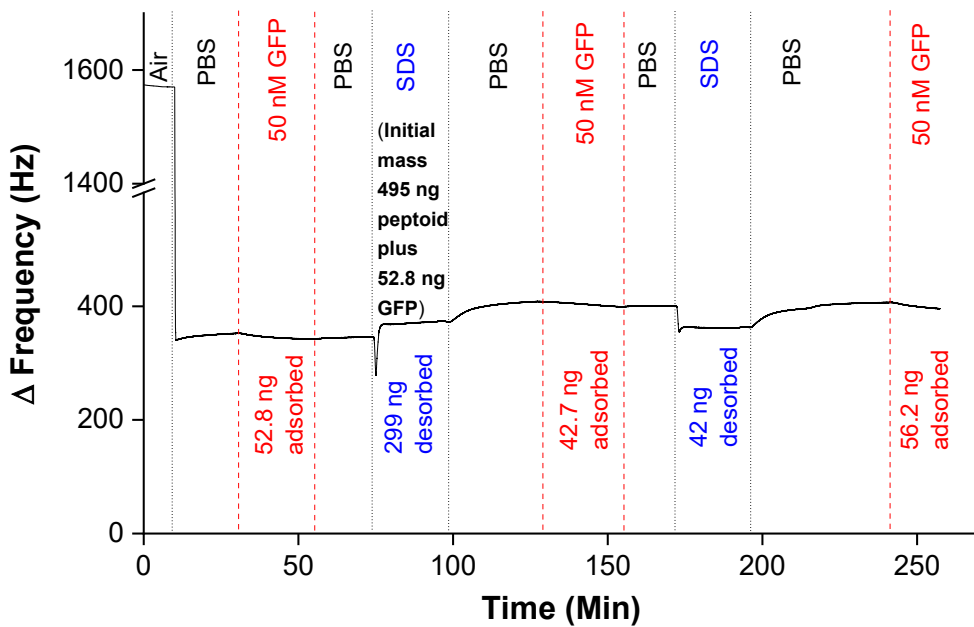
Figure S6. Reusability experiment for IOS-1 peptoid-based immunobiosensor
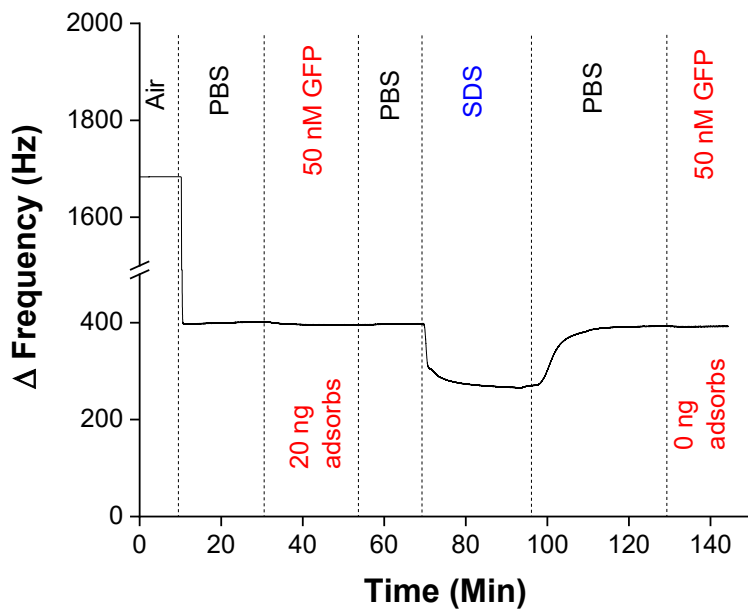

Figure S7. Reusability experiment for anti-GFP antibody-based immunobiosensor
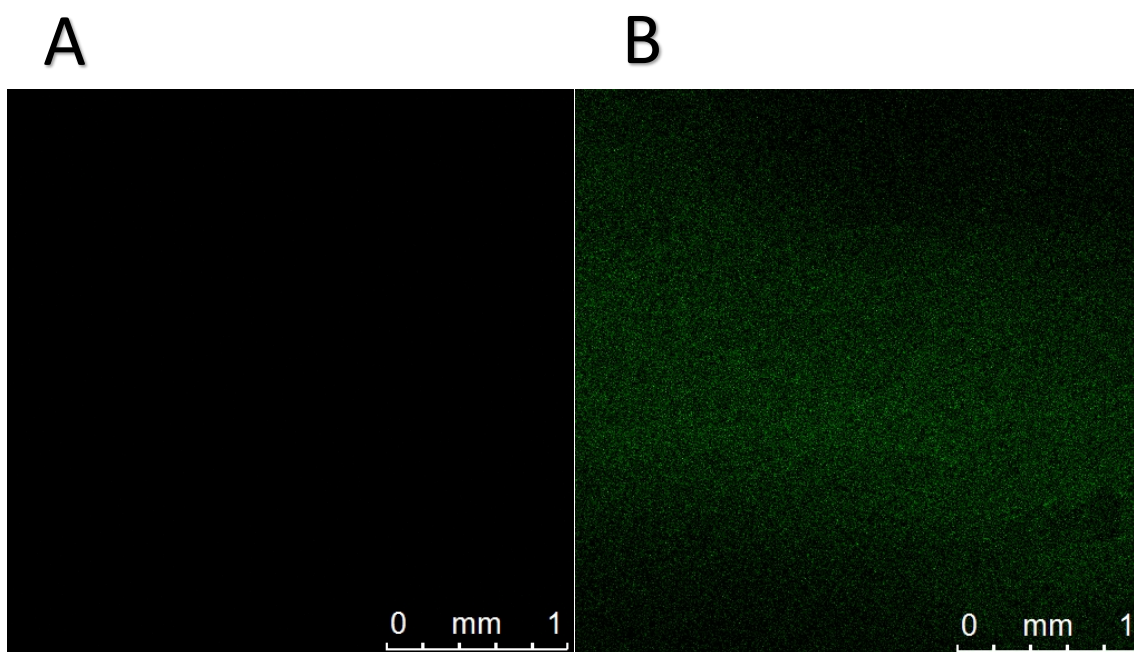
Figure S8. (A) Fluorescent microscope image of IOS-1 peptoid modified Au sensor. **(B)** Fluorescent microscope image of GFP immobilized on IOS-1 peptoid modified Au sensor.
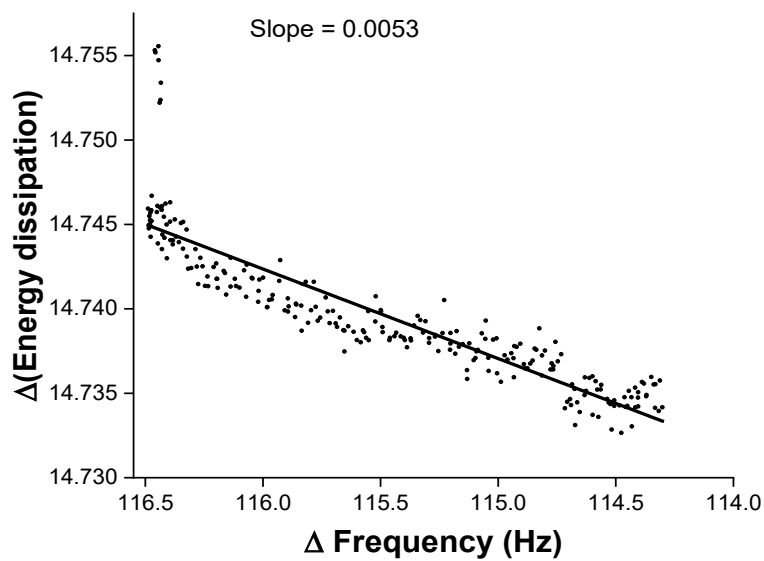

Figure S9. Slope of change in energy dissipation versus change in frequency for clean sensor
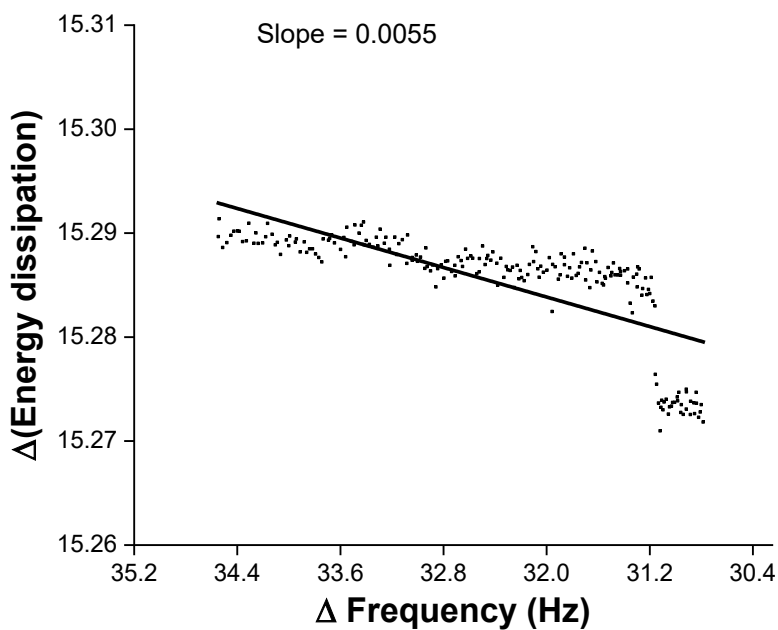
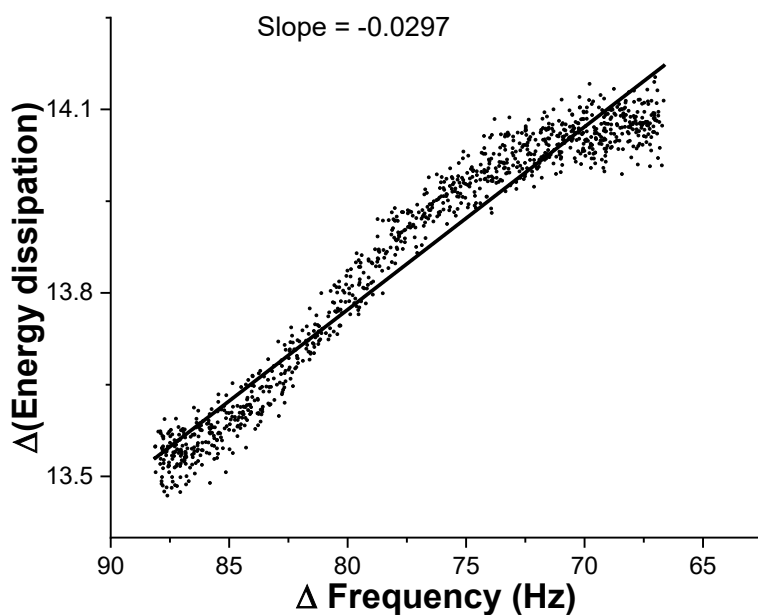**Figure S10.** The slope of change in energy dissipation versus change in frequency for IOS-1 peptoid

Figure S11. Slope of change in energy dissipation versus change in frequency for GFP protein
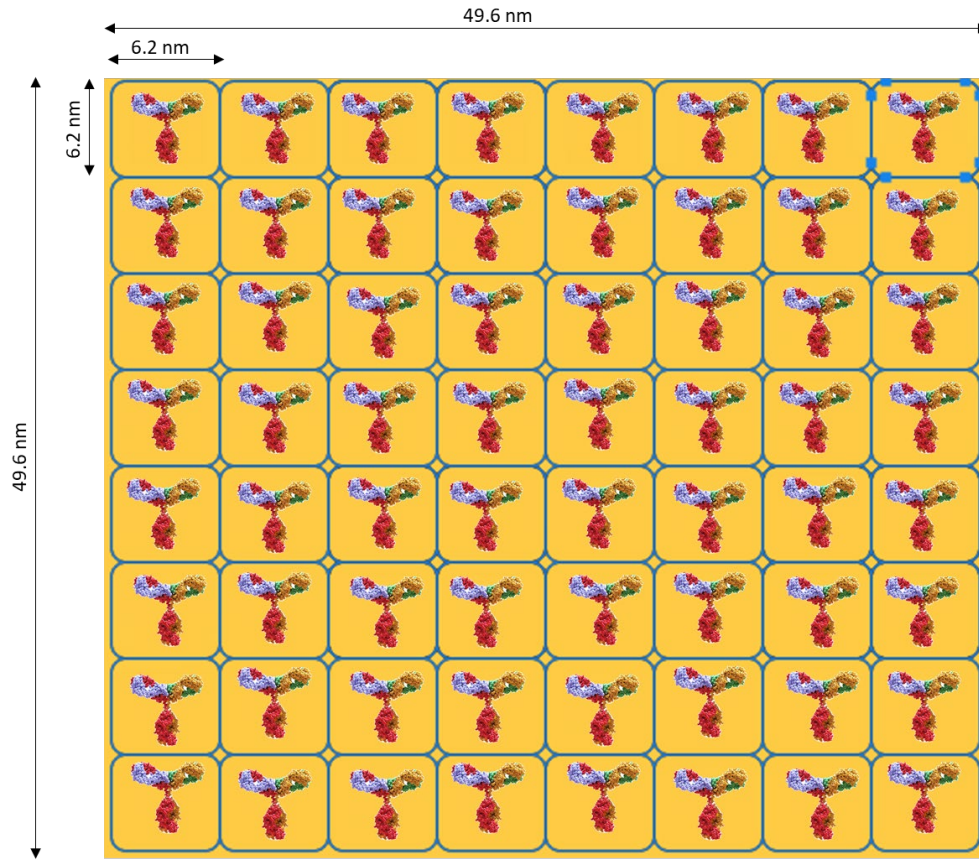
Figure S12. Illustration of binding sites per unit area of GFP antibody immunobiosensor

Antibody cross-sectional area = 38.5 nm^2

Au surface => 2460 nm^2 or 0.0025 μm^2

Antibody molecular weight = 150000 g/mol

1 mole of antibody = 6x10^{23} molecules

GFP antibody => 2.5X10^{-10} ng per molecule

64 antibody molecules => 2460 nm^2 of surface

Binding site per antibody molecule = 2

Binding sites per 2460 nm^2 surface = 128

QCM sensor => 0.78 cm^2 = 7.8x1013 nm^2

QCM sensor => 2.03x10^{12} antibody molecules

Figure S13. Illustration of binding sites per unit area of IOS-1 peptoid immunobiosensor

IOS-1 peptoid cross-sectional area = 0.733 nm^2

38.5 nm^2 of Au surface => 8 peptoid molecules

IOS-1 peptoid molecular weight = 1364 g/mol

1 mole of IOS-1 peptoid = 6x10^{23} molecules

IOS-1 peptoid => 2.27X10^{-12} ng per molecule

512 IOS-1 peptoid molecules => 2460 nm^2

Min. binding sites per IOS-1 peptoid molecule = 1

Min. binding sites per 2460 nm^2 surface = 512

QCM sensor => 0.78 cm^2 = 7.8x10^{13} nm^2

QCM sensor => 1.62x10^{13} IOS-1 peptoid molecules

Table S1. Theoretical mass of molecules for 2D-monolayer coverage of the QCM sensor.

Mass of GFP aB for monolayer coverage of 1cm diameter QCM Sensor				
Surface area of sensor in square cm	0.79			
C/S area of GFP antibody in square nanometers	38.5			
C/S area of GFP antibody molecule in square cm	3.85E-13			
Height of monolayer (nm)	14			
Molecular mass (g/mol)	150000		Av. No.	6E+23
Number of GFP antibody required to form monolayer	2.05195E+12			
Mass required to form monolayer (moles)	3.40855E-12			
Mass required to form monolayer (grams)	5.11283E-07			
Mass required to form monolayer (Micrograms)	0.511	511 ng		

Mass of IOS peptoid required for monolayer coverage of QCM Gold Sensor				
Area of sensor in square cm	0.79			
C/S area of peptoid in square nanometers	0.733			
C/S area of peptoid in square cm	7.33E-15			
Height of monolayer (cm)	1.558E-07			
Molecular mass (kDa)	1.364	1364 g/mol	Av. No.	6E+23
Number of peptoid molecules reqd. for monolayer	1.07776E+14			
Mass required to form monolayer (moles)	1.7903E-10	1.7903E-10		
Mass required to form monolayer (grams)	2.44197E-07	2.44E-07		
Mass required to form monolayer (Micrograms)	2.442E-01	244 ng		

Mass of DSS required for monolayer coverage of 1cm diameter QCM Gold Sensor				
Area of sensor in square cm	0.79			
Area of DSS in square nanometers	0.178			
Area of DSS in square cm	1.78E-15			
Height of monolayer (cm)	4.75E-08			
Molecular mass (kDa)	0.36835	368.35 g/mol	Av. No.	6E+23
Number of DSS required to form monolayer	4.4382E+14			
Mass required to form monolayer (moles)	7.37243E-10	7.3724E-10		
Mass required to form monolayer (grams)	2.71416E-07	2.71E-07		
Mass required to form monolayer (Micrograms)	0.271	271 ng		

Mass of cysteamine required for monolayer coverage of 1cm diameter QCM Gold Sensor				
Area of sensor in square cm	0.79			
Area of cysteamine in square nanometers	0.068			
Area of cysteamine in square cm	6.8E-16			
Height of monolayer (cm)	0.00000003			
Molecular mass (kDa)	0.077	77.15 g/mol	Av. No.	6E+23
Number of antibody required to form monolayer	1.16176E+15			
Mass required to form monolayer (moles)	1.92984E-09	1.9298E-09		
Mass required to form monolayer (grams)	1.48887E-07	1.49E-07		
Mass required to form monolayer (Micrograms)	0.149	149 ng		

Sauerbrey's equation

The mass of material that adsorbs/desorbs from a QCM sensor can be quantified using the Sauerbrey equation. Sauerbrey relates the mass change (ΔM) to the frequency shift (Δf) as follows:

$$\Delta M = \frac{c}{n}\Delta f \qquad\qquad \text{................... (1)}$$

where n is the harmonic or overtone number, t_q is the thickness of the quartz crystal, ρ_q is the density of quartz and f_0 represents the resonant frequency of the sensor. C = -17.7 Hz ng/cm^2 for a 5-MHz crystal.[36]